JGR Solid Earth

RESEARCH ARTICLE

10.1029/2025JB032147

Key Points:

- A new 3D attenuation model is obtained for the crustal and uppermost mantle in the Indo-Burma subduction zone
- High attenuation is observed in the Central Myanmar Basin and the mid-lower crust beneath the Indo-Burma Ranges
- Asthenospheric upwelling triggered by the Indian plate retreat/tearing may heat the cold lithospheric mantle and feed the Monywa volcano

Supporting Information:

Supporting Information may be found in the online version of this article.

Correspondence to:

Y. Ai,
ysai@mail.iggcas.ac.cn

Citation:

Feng, Y., Ai, Y., De Siena, L., He, Y., Jiang, M., Mon, C. T., et al. (2026). Seismic attenuation tomography in Central Myanmar and its implications on continental subduction and arc magmatism. *Journal of Geophysical Research: Solid Earth*, *131*, e2025JB032147. https://doi.org/10.1029/2025JB032147

Received 8 JUN 2025
Accepted 12 JAN 2026

Author Contributions:

Data curation: Yilin Feng, Yinshuang Ai, Yumei He, Mingming Jiang, Chit Thet Mon, Yiming Bai, Guangbing Hou, Yuan Ling, Myo Thant, Kyaing Sein
Formal analysis: Yilin Feng
Funding acquisition: Yinshuang Ai, Yumei He
Investigation: Yilin Feng, Yinshuang Ai
Methodology: Yilin Feng, Yinshuang Ai, Luca De Siena, Simona Gabrielli, Ferdinando Napolitano
Project administration: Yinshuang Ai
Resources: Yilin Feng, Yinshuang Ai, Yumei He, Mingming Jiang, Chit Thet Mon, Yiming Bai, Guangbing Hou, Yuan Ling, Myo Thant, Kyaing Sein
Software: Luca De Siena, Simona Gabrielli, Ferdinando Napolitano
Supervision: Yinshuang Ai

Seismic Attenuation Tomography in Central Myanmar and Its Implications on Continental Subduction and Arc Magmatism

Yilin Feng[1,2], Yinshuang Ai[1,2,3], Luca De Siena[4], Yumei He[1], Mingming Jiang[1,2], Chit Thet Mon[1], Lian-Feng Zhao[1], Yiming Bai[5], Guangbing Hou[1], Yuan Ling[1], Simona Gabrielli[6], Ferdinando Napolitano[7], Myo Thant[8], and Kyaing Sein[9]

[1]Key Laboratory of Planetary Science and Frontier Technology, Institute of Geology and Geophysics, Chinese Academy of Sciences, Beijing, China, [2]University of Chinese Academy of Sciences, Beijing, China, [3]Mohe Observatory of Geophysics, Institute of Geology and Geophysics, Chinese Academy of Sciences, Beijing, China, [4]Dipartimento di Fisica e Astronomia (DIFA), Alma Mater Studiorum-Università di Bologna, Bologna, Italy, [5]Division of Mathematical Sciences, School of Physical and Mathematical Sciences, Nanyang Technological University, Singapore, Singapore, [6]Istituto Nazionale di Geofisica e Vulcanologia, Rome, Italy, [7]Department of Physics "E.R. Caianiello," University of Salerno, Fisciano, Italy, [8]Department of Geology, University of Yangon, Yangon, Myanmar, [9]Myanmar Geosciences Society, Yangon, Myanmar

Abstract Myanmar is located on the eastern margin of the India-Eurasia collision zone, where the Indian sub-continent is subducting beneath the Burma microplate. Magmatic processes during subduction and collision in orogenic belts are significant and well-studied for oceanic subduction; however, the magmatism associated with continental subduction remains poorly understood. Seismic attenuation is highly sensitive to changes in lithospheric thermodynamics and fluid content. Understanding arc volcanism is vital for comprehending a key manifestation of subduction-related processes. However, there is still no high-resolution 3D attenuation model for this region. Here, we use the coda-normalized method to image the lithospheric-scale 3D attenuation structure in the Indo-Burma subduction zone. Our results reveal high attenuation in major sedimentary basins. The prominent high-attenuation anomalies in the mid-to-lower crust of the Indo-Burma Ranges (IBR) may represent thick, fluid-rich sediments scraped off from the subducting Indian Plate and accumulated beneath the IBR. Low-attenuation anomalies at depths of 30–50 km beneath the Monywa volcano are a clear signature of a cooled mantle wedge, which currently overlies strong attenuation anomalies deeper than 50 km, likely associated with the upwelling of hot asthenospheric material. Compared to oceanic subduction systems, the insufficient water content of the continental subduction plate, coupled with the compressional regime induced by oblique subduction, leads to weak attenuation within the mantle wedge.

Plain Language Summary Seismic attenuation tomography is a powerful technique for understanding the subsurface thermal structure. Previous studies have constructed 3D seismic velocity models at multiple scales beneath Myanmar; however, a high-resolution 3D attenuation model remains lacking. In this study, we adopt the coda-normalized method to investigate the attenuation structure in the crust and uppermost mantle beneath central Myanmar. The resulting model shows high attenuation in the central Myanmar Basin. High attenuation appears in the mid-to-lower crust beneath the Indo-Burma Ranges. The primary low-attenuation anomaly marks the crust-mantle boundary across the fore-arc and back-arc basins. It is a signature of cooled mantle, which, at depths of 30–50 km, underlies the high-attenuation system of the Monywa volcanic area. At 22°N latitude, a high-attenuation anomaly parallel to the subducting slab is observed, which may result from slab dehydration inducing limited partial melting above the slab. This feature, at our resolution, appears disconnected from the upper volcanic systems. Therefore, we infer the possible presence of a narrow conduit that facilitates the transport of fluids and melts, feeding the Monywa volcanic system.

1. Introduction

Following the Eocene continent-continent collision between the Indian and Eurasian plates, the large-scale subduction of the Indian continental lithosphere beneath Eurasia has driven the present-day geodynamic processes, including regional tectonics and arc-related magmatism, along the Indo-Burma oblique convergence margin (Y. Wang et al., 2014). In the context of plate collision and subduction, Myanmar can be broadly divided into four tectonic regimes from west to east: (a) the Indo-Burma Ranges (IBR), which were formed primarily

Visualization: Yilin Feng, Yinshuang Ai, Lian-Feng Zhao
Writing – original draft: Yilin Feng, Yinshuang Ai
Writing – review & editing: Yilin Feng, Yinshuang Ai, Luca De Siena, Yumei He, Mingming Jiang, Chit Thet Mon, Lian-Feng Zhao, Yiming Bai, Simona Gabrielli, Ferdinando Napolitano

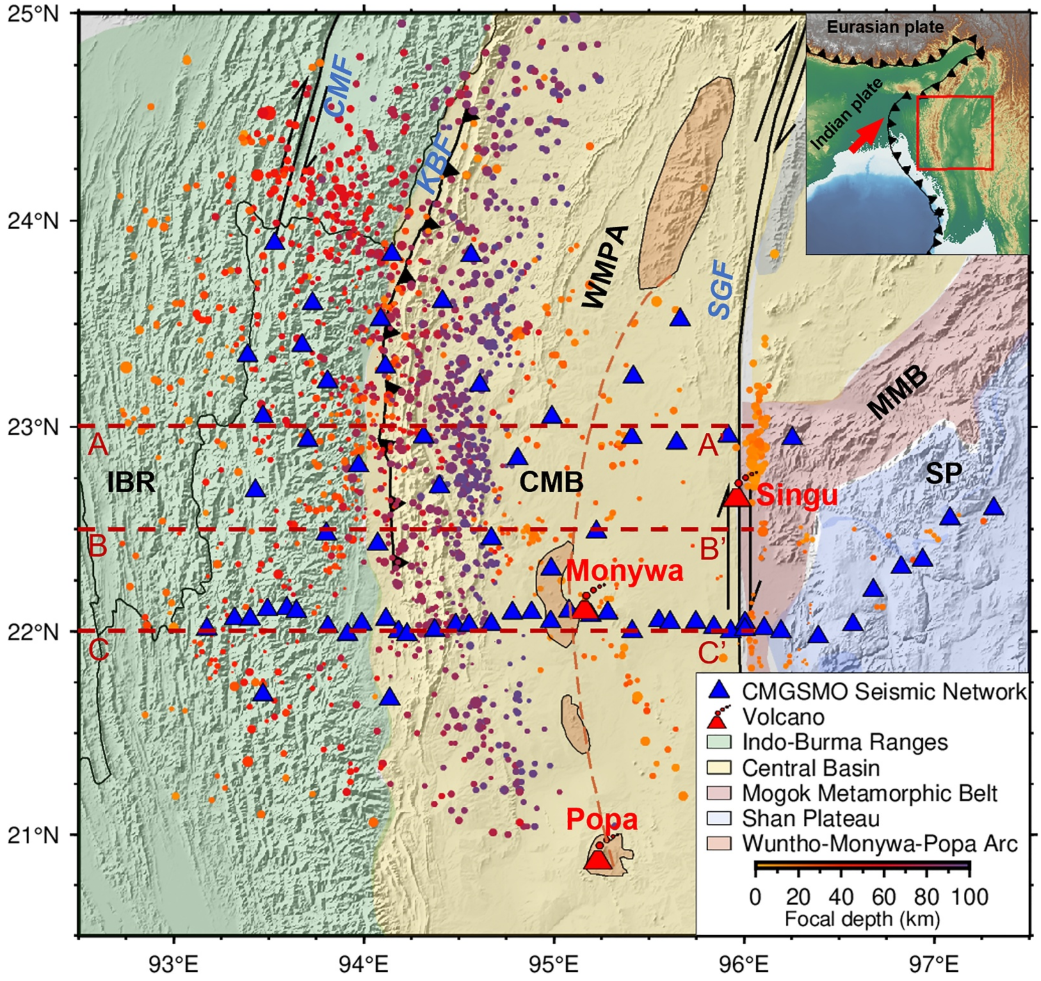

Figure 1. Simplified tectonic map of the Myanmar region, illustrating major tectonic blocks, seismic stations, seismic events, and major faults. Major geological units are distinguished by color: the Indo-Burma Ranges in green, the Central Myanmar Basin in yellow, the Wuntho-Monywa-Popa arc (WMPA) in dark orange, the Mogok Metamorphic Belt in pink, and the Shan Plateau in cyan. Major volcanoes (i.e., Popa, Monywa, and Singu) are marked. Blue triangles denote the seismic stations in the CMGSMO seismic network. Seismicity is plotted as dots colored by focal depth. Major faults, including the Churachandpur-Mao Fault, Kabaw Fault, and Sagaing Fault, are plotted with north-south trending black lines. The west-east trending dashed red line indicates the traces of the profiles presented in Figure 4. The inset map in the top right corner illustrates the location of the study region within the broader Indo-Eurasia collision system.

during the late Neogene by fast accretion of the Bengal Basin sediments, can be further divided into outer, inner and core zones (Morley et al., 2020); (b) the Central Myanmar Basin (CMB), comprising a series of Cenozoic basins filled with up to 15 km of Eocene-to-Pliocene sediments, is split into a fore- and back-arc by the north-south trending Wuntho-Monywa-Popa arc (WMPA) (Cai et al., 2020), which is characterized by predominantly Late Cretaceous to Tertiary granodioritic batholiths and subordinate Late Cretaceous to Quaternary volcanic rocks (Maurin & Rangin, 2009; Mitchell et al., 2012; Pivnik et al., 1998); the Monywa volcano (MWV) is located at the center of this arc; (c) the Mogok Metamorphic Belt, a roughly N-S trending belt of low- and high-grade metamorphic, ultramafic, and Jurassic to Miocene S-type intrusive rocks (Licht et al., 2020); and (d) the Shan Plateau (SP), consisting of Paleozoic and Mesozoic meta-sedimentary rocks attributed to the Sibumasu Terrane of Sundaland (Metcalfe, 2013) (Figure 1). To comprehensively understand the complex tectonic evolution at the east margin of the Indian plate and its relationship to seismicity and volcanism, it is essential to model seismic structures beneath Myanmar.

The 3D structure, seismotectonics, and volcanism of the central Myanmar region have been clarified by several 3D seismic tomography studies beneath the Indo-Burma subduction zone (IBSZ) and its surroundings (Bai et al., 2021; Tian et al., 2024; X. Wang et al., 2019; S. Wu et al., 2021; G. Zhang et al., 2021). These studies have revealed high lateral heterogeneity in seismic velocity in the IBSZ, providing insights into the subducting slab geometry and the extension of the accretionary wedge and arc magmatism. The IBSZ involves the subduction of continental lithosphere, as evidenced by low seismic velocities across a slab of approximately 30 km in thickness (G. Zhang et al., 2021; T. Zheng et al., 2020). Crustal low-velocity anomalies in the IBR likely mark the Bengal sediments accreted to the toe of the overlying Burma plate (Bai et al., 2021). Furthermore, the CMB exhibits low velocities and high Vp/Vs ratios, potentially indicative of fluid-saturated sediments (Bai et al., 2021; G. Zhang et al., 2021). The origin of the MWV remains debated. A low-velocity body beneath the volcanic arc was identified by G. Zhang et al. (2021), Bai et al. (2021), and T. Zheng et al. (2020) and interpreted as a molten reservoir feeding the volcanic system. On the other hand, S. Wu et al. (2021) observe no significant crustal or mantle low-velocity body beneath MWV.

Other studies have focused on volcanic activity in the region. Geochemical investigations of volcanic rocks from the study area, including isotopic dating, major element analysis, and petrographic characterization, suggest a two-stage magmatic evolution (Lee et al., 2016). High-potassium calc-alkaline compositions, indicative of subduction-related magmatism, characterize Middle Miocene volcanic rocks. The subsequent Quaternary basaltic volcanism is inferred to be derived from partial melting of the asthenosphere (Lee et al., 2016; Licht et al., 2020; L. Y. Zhang et al., 2020). To further explore the deep geodynamic processes underlying magmatic evolution, Rao et al. (2014) have employed the magnetotelluric method to image the crust–mantle conductivity structure. A high-conductivity zone representative of fluids was identified at latitude 22.25° and depths of 50–60 km (Rao et al., 2014). Both the origin and pathways of magmatic materials remain uncertain due to the lack of well-defined constraints on the subsurface structure.

Seismic velocity is primarily sensitive to the elastic properties of the Earth. The sensitivity of seismic attenuation to thermally- and fluid-induced processes offers distinct advantages for investigating lithospheric structures and magmatism. At the lithospheric scale, seismic attenuation shows high sensitivity to temperature changes and pathways of melt and fluids from the subducting plate to volcanic centers (Boyd et al., 2004; Schurr et al., 2003). Elevated temperatures and high melt content can induce strong intrinsic seismic attenuation, providing a valuable window into geodynamic processes beneath volcanic arcs. To date, the attenuation structure of the IBSZ remains unexplored. He et al. (2021) have investigated the Lg-wave attenuation structure in the southeastern margin of the Tibetan Plateau; however, this method is sensitive to lateral variations but lacks sufficient depth resolution. Additionally, the limited number of near-source seismic arrays in Myanmar results in sparse data coverage, hindering a detailed interpretation of the subsurface structure in the region. Investigating the characteristics of 3D attenuation structure beneath central Myanmar is thus crucial for constraining regional tectonics, their thermal characteristics, and dynamic evolution.

The coda-normalization (CN) method utilizes late-lapse-time coda wave energies to normalize direct-wave energies, thereby effectively removing source, site, and instrument effects from path-dependent attenuation measurements (Sato et al., 2012). The CN method is today a standard technique in attenuation tomography for both volcanic (De Siena et al., 2014; De Siena, Amoruso, et al., 2017, De Siena, Chiodini, 2017; Del Pezzo et al., 2006; Prudencio et al., 2015) and tectonic settings (Borleanu et al., 2023; Gabrielli et al., 2025; Sketsiou et al., 2021). Based on this method, this study presents a detailed 3D S-wave attenuation model for the IBSZ. By integrating our new model with geochemical analyses of surface volcanic rocks and other geophysical observations, we provide constraints on the thermal structure of the crust and uppermost mantle, thereby improving our understanding of geodynamic and magmatic processes in the IBSZ.

2. Data and Method

2.1. Data

This study utilizes high-quality waveform data from local earthquakes recorded by the CMGSMO (the China-Myanmar Geophysical Survey in the Myanmar Orogen) seismic array, which comprised 71 temporary seismic stations deployed within the study area (latitude: 21.0°N–25.0°N, longitude: 92.5°E−97.5°E, Figure 1) between June 2016 and February 2018 (Feng et al., 2025). The array consists of a dense, east-west-trending linear subarray with a station spacing of 10–15 km, and a 2D backbone network with a spacing of 30–50 km.

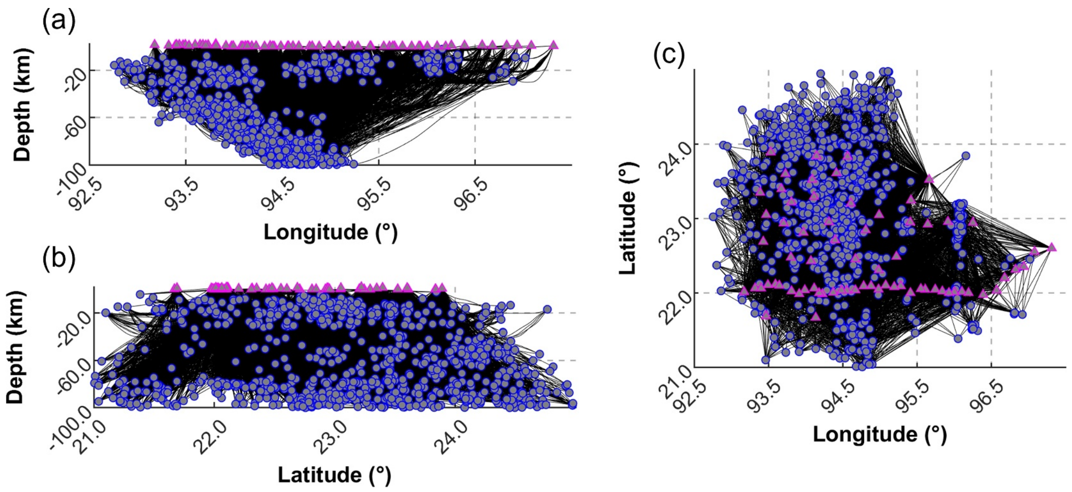

Figure 2. Raypath coverage in different projections: (a) projection onto a longitude–depth cross-section, (b) projection onto a latitude–depth cross-section, and (c) projection onto the surface (latitude–longitude plane). Triangles and circles indicate stations and seismic events, respectively.

We utilized manually selected earthquake events by Mon et al. (2020, 2023). To ensure data robustness, we selected only events with local magnitudes ranging from 2 to 4 and focal depths of ≤100 km, because aftershocks often occur in the coda waves of large-magnitude earthquakes (De Siena et al., 2009). Each event should be recorded by at least 8 stations. Following preprocessing and quality control of the available waveforms, the final data set comprises 1,832 earthquakes and 59,565 waveforms. The 3D ray paths were traced using the pseudo-bending method (Um & Thurber, 1987). Figure 2 shows the ray path coverage for these events, indicating sufficient ray coverage in the crust beneath the study area. While ray coverage diminishes with increasing depth, a substantial portion of earthquakes occur within the 50–100 km depth range (Figure 2a), providing valuable constraints for depicting the subducting Indian lithosphere beneath Myanmar.

2.2. The Coda-Normalization Method

The CN method normalizes P- and S-wave energy for coda energy (Aki, 1980; Yoshimoto et al., 1993). Consistent with most body-wave attenuation tomography approaches, the CN method used in this study measures total attenuation without separating the intrinsic and scattering attenuation. Seismic wave energies can be modeled as the convolution of the source, path, site, and instrument functions, allowing the spectral energy of direct waves to be

$$E(f,r) = R_{\theta\phi} S_s(f)\, r^{-\gamma} I(f)\, G(f,\Psi)\, \exp\left(-\frac{2\pi f}{Q(f)\, v} r\right), \tag{1}$$

where f is the frequency, r is the source-receiver distance, $R_{\theta\phi}$ is the source radiation pattern (θ and ϕ denote the azimuth and take-off angle for a source-receiver ray, respectively), $S_s(f)$ is the source function, γ is the geometrical spreading exponent, $I(f)$ is the known instrumental response, $G(f,\Psi)$ is the site amplification factor (with Ψ being the incident angle of the ray at the station), Q is the direct-wave quality factor and v is the average velocity in the medium (Yoshimoto et al., 1993).

The spectral energy of coda waves E_c can be written as

$$E_c(f,t_c) = S_s(f)\, P(f,t_c)\, G(f)\, I(f), \tag{2}$$

where t_c is the coda-wave central lapse time from the origin time of the event t_0.

The attenuation of coda waves can then be expressed as (Aki & Chouet, 1975)

$$P(f,t_c) = t_c^{-n}\exp\left(-2\pi f Q_c^{-1} t_c\right), \tag{3}$$

In this equation, n is the envelope spectral decay, Q_c is the coda quality factor, and $P\,(f,\,t_c)$ does not include the effect of the source radiation pattern. Equation 1 can be divided by Equation 2 to normalize the spectral energy of direct waves using the spectral energy of coda waves

$$\frac{E(f,r)}{R_{\theta\phi}E_c\,(f,t_c)} = r^{-\gamma}\frac{G(f,\Psi)}{G(f)}\exp\left(-\frac{2\pi f}{Q(f)\,v}r\right)\frac{1}{P(f,t_c)}, \tag{4}$$

where the source function $S_s(f)$ and the instrumental response $I(f)$ contributions disappear. By measuring direct-wave energy over a window of sufficient length t_l, we smooth the azimuthal contribution of the radiation pattern (De Siena et al., 2009, 2010). If the length of the direct-wave window is chosen appropriately, the contribution of the source radiation pattern $R_{\theta\phi}$ is negligible (De Siena et al., 2009) so that $R_{\theta\phi} = 1$ and $\frac{G(f,\Psi)}{G(f)} = 1$. Since the early coda consists of randomly scattered waves, the coherency and source radiation pattern are eventually lost (Takemura et al., 2009). De Siena et al. (2010) demonstrate that a body-wave window of 2 s is sufficient to make the radiation pattern quasi-isotropic in a volcanic caldera. Still, the window length must be carefully chosen at each frequency to avoid the near-receiver onset of surface waves (Gabrielli et al., 2020): at our scale and frequencies, a body-wave window of 3 s mitigates differences in radiation pattern (De Siena et al., 2009). At a fixed frequency band and starting lapse-time for coda windows, $P(f,\,t_c)$ is assumed to be constant in the standard CN method (Del Pezzo et al., 2006; Sato et al., 2012). Taking the logarithm, Equation 4 becomes

$$\ln\left(\frac{E(f,r)}{E_c\,(f,t_c)}\right) = -\ln P(f,t_c) - \gamma\ln(r) - \frac{2\pi f}{Q(f)\,v}r, \tag{5}$$

a linear equation solved for three unknowns ($\ln P(f,\,t_c)$, r, Q) once the hypocentral distance is known and the frequency is set. If Q_c is measured for each source station pair, one can pre-estimate $P(f,\,t_c)$ using Equation 3, as done by De Siena, Amoruso, et al. (2017), De Siena, Chiodini, et al. (2017):

$$\frac{1}{2\pi f}\ln\frac{E(f,t_c)}{E_c\,(f,t_c)} + \frac{1}{2\pi f}\ln P(f,t_c) = -\frac{\gamma\ln(r)}{2\pi f} - Q(f)^{-1}t. \tag{6}$$

The system can be solved with a linear inversion for r and $Q(f)^{-1}$, and we calculate the theoretical energy ratio.

$$\left[\frac{1}{2\pi f}\ln\frac{E(f,t_c)}{E_c\,(f,t_c)}\right]_{\text{theoretical}} = \frac{1}{2\pi f}\ln P(f,t_c) - \frac{\gamma_{\text{average}}\ln(r)}{2\pi f} - Q(f)^{-1}_{\text{average}}t. \tag{7}$$

Then, we invert for the attenuation value ΔQ^{-1} along the seismic ray path based on the difference between the theoretical energy ratio and the observed energy ratio.

$$\left[\frac{1}{2\pi f}\ln\frac{E(f,t_c)}{E_c\,(f,t_c)}\right]_{\text{real}} - \left[\frac{1}{2\pi f}\ln\frac{E(f,t_c)}{E_c\,(f,t_c)}\right]_{\text{theoretical}} = G\Delta Q^{-1}. \tag{8}$$

The iterative inversion method is used to obtain the relative inverse attenuation value of each mesh. The inversion was performed using a 3D regular grid, with a horizontal spacing of 0.5° × 0.5° and a vertical spacing of 10 km, since the average station spacing in the CMGSMO seismic network is approximately 30–50 km. This resolution was determined by considering the station distribution density and ray-path coverage, ensuring model stability while allowing us to resolve the main spatial variations as much as possible.

Building on Equation 8, we express the difference between the observed and theoretical energy ratios as a linear system, where the matrix G contains the path-dependent sensitivity kernels and the model vector consists of the unknown attenuation perturbations ΔQ^{-1}. This allows us to reformulate the problem as a damped least-squares inversion:

$$\min_{\Delta Q^{-1}} \|G\Delta Q^{-1} - d\|_2^2 + \epsilon^2 \|L\Delta Q^{-1}\|_2^2, \tag{9}$$

where d is the data vector derived from the left-hand side of Equation 8, L is the regularization matrix, and ϵ is the damping parameter controlling the trade-off between data misfit and model smoothness.

To solve this ill-posed problem, we apply the conjugate gradient least-squares algorithm, adding a positivity constraint on total attenuation values. The optimal damping parameter ϵ is selected using the L-curve criterion, ensuring a balance between stability and resolution (Figure S1 in Supporting Information S1). The resulting solution provides the path-dependent attenuation distribution, which is subsequently mapped onto a 3D grid to obtain the final attenuation tomography model.

2.3. Data Processing

A 3-s time window before the P-wave arrival was selected to calculate noise, and a 3-s window after the S-wave arrival for S-wave energies, as exemplified in Figure S2 in Supporting Information S1. The frequency-distribution plot of S-wave arrival time was calculated to determine a coda time window starting 60 s after the event origin, with a window length of 35 s. The lengths of the body-wave, noise, and coda windows were determined from both reference studies and empirical tests (De Siena et al., 2014). A 3-s body-wave and noise window effectively averages radiation-pattern effects and captures stable noise levels, while a 35-s coda window provides sufficient duration to sample stable coda energy for imaging the crust and uppermost mantle (Figures S3–S5 in Supporting Information S1). The envelope energy was integrated over three distinct time windows (noise, S-wave, and coda), and each was normalized by its corresponding window length. Subsequently, the energy ratios of body-to-coda and coda-to-noise were calculated. Seismic waveforms were retained only if the coda-to-noise ratio exceeded 3.0. The center frequency for each ray was calculated (Figure S6 in Supporting Information S1) to map the energy distribution across different frequencies, facilitating the selection of frequencies with concentrated energy for subsequent analyses.

3. Results

3.1. Attenuation Tomography Models

Figure 3 presents horizontal cross-sections of relative Q_s^{-1} values, which represent the variation relative to the average inverse Q, at depths ranging from 10 to 60 km. Figure 4 illustrates vertical cross-sections at latitudes 23°, 22.5°, and 22°N, displaying variations from north to south. In the upper crust (Figure 3a), a high-attenuation anomaly is mainly observed beneath the CMB. In the middle crust (Figure 3b), high attenuation persists beneath the CMB, with the anomaly migrating westward as depth increases. The pattern is potentially linked to variations in the thickness of the fore-arc and back-arc sedimentary sequences. The high-attenuation anomaly (HA1) beneath the CMB, evident in the 22°N vertical profile (Figure 4c), exhibits higher attenuation anomalies in the fore-arc region than in the back-arc region. A north-south trending zone of high attenuation appears exclusively under the IBR in the lower crust, identified elsewhere as the crust-mantle boundary. Compared with the upper and middle crust results, attenuation in the lower crust increases significantly in this region.

In the uppermost mantle, low-attenuation anomalies are visible beneath the volcanic arc at the top of the upper mantle (Figures 3c–3e). This inference is supported by the presence of low-attenuation anomalies (LA1) beneath the volcanic arc across the three vertical profiles in Figures 4a–4c. Furthermore, we observe a distinct, north-south trending zone of high attenuation gradually developing from west to east within the lithospheric mantle. Along the 22°N profile (Figure 4c), this corresponds to a high attenuation anomaly observed along and above the subducting slab. This strong attenuation anomaly (HA2) diminishes with increasing latitude. A high-attenuation (HA3) zone, located beneath the subducting plate at depths between 60 and 80 km (Figure 4c), under the volcanic arc, likely marks the upwelling of hot, asthenospheric material. However, no direct high- or moderate-attenuation pathway connects this wedge to the volcanic arc, unlike typical oceanic subduction settings (Schurr et al., 2003).

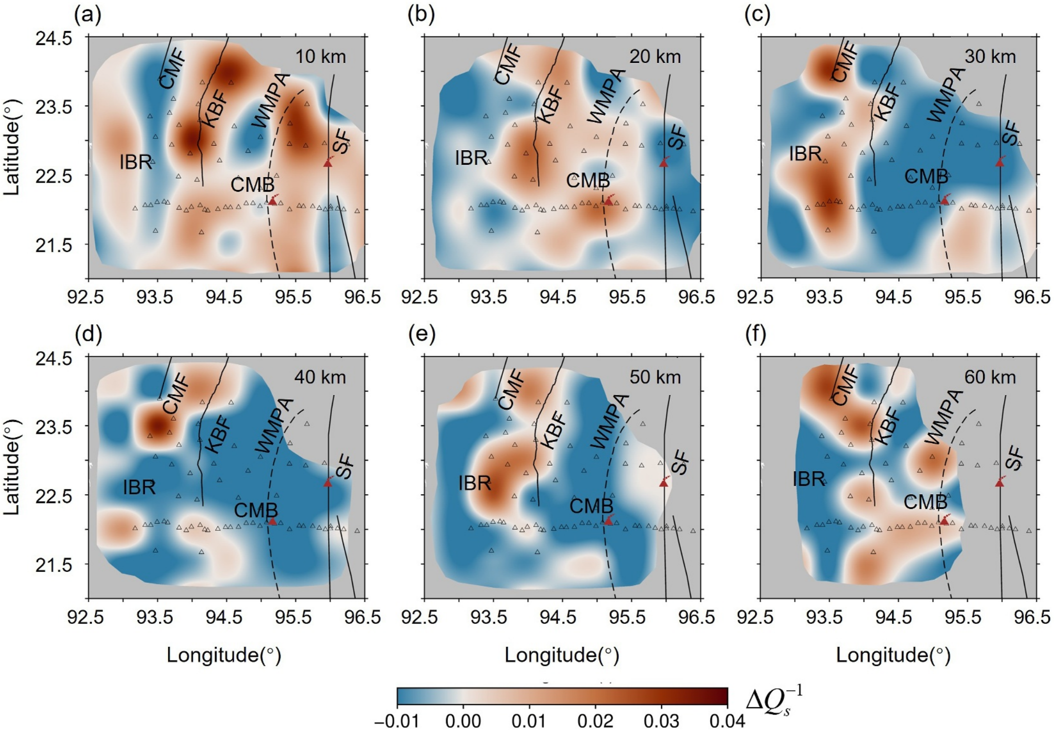

Figure 3. Horizontal cross-sections of the relative attenuation value of the S-wave at (a) 10 km, (b) 20 km, (c) 30 km, (d) 40 km, (e) 50 km, and (f) 60 km depths. The main faults, including the Churachandpur-Mao Fault, Kabaw Fault, and Sagaing Fault (SF), are shown as black lines. The dashed black lines delineate the WMPA. The black triangles are seismic stations. Areas with limited resolution are clipped.

3.2. Synthetic Tests

To assess the reliability of our results, we first performed a recovery test. Specifically, we used the anomalous region identified by the tomographic inversion as the input model. We conducted an inversion experiment using the same method and parameter settings as the actual inversion process. The results, shown in Figures S4 and S5 in Supporting Information S1, demonstrate that the main features identified by the tomographic inversion can be effectively recovered. This provides strong support for the robustness and reliability of our inversion results.

To evaluate the robustness of our imaging results, we also performed a suite of checkerboard tests. Gaussian noise with zero mean and a standard deviation of 0.2 was added to the synthetic data and subsequently inverted using the same parameters (including the damping factor and grid size) as those employed for the observed data. The results of the checkerboard tests at various depth profiles are presented in Figure 5 with anomaly sizes of 0.5° × 0.5°. Additional checkerboard test results across latitude profiles are shown in Figure S9 in Supporting Information S1. Anomalies are well-resolved in the central study area and areas of interest, including the CMB and inner IBR. In contrast, anomalies become smeared and distorted towards the marginal regions, such as the SP and the outer IBR, where data coverage is less sufficient. We also assessed the stability of our attenuation measurements by explicitly verifying that the logarithm of the total coda-normalized S-wave amplitude decreases with increasing travel time (Figure 6). If the CN model is valid, both the right-hand side and left-hand side of Equation 5 show a negative linear relationship with the direct-wave travel times (De Siena et al., 2014). In Figure 6, black dots represent amplitude ratios derived from observational data, while red circles depict the theoretical attenuation values calculated post-inversion, based on the averaged attenuation and geometrical spreading. Furthermore, we computed the residuals between the observed and theoretical attenuation values (Figure S10 in Supporting Information S1). The residuals, which represent the differences between observed and predicted energy ratio, follow an approximately normal

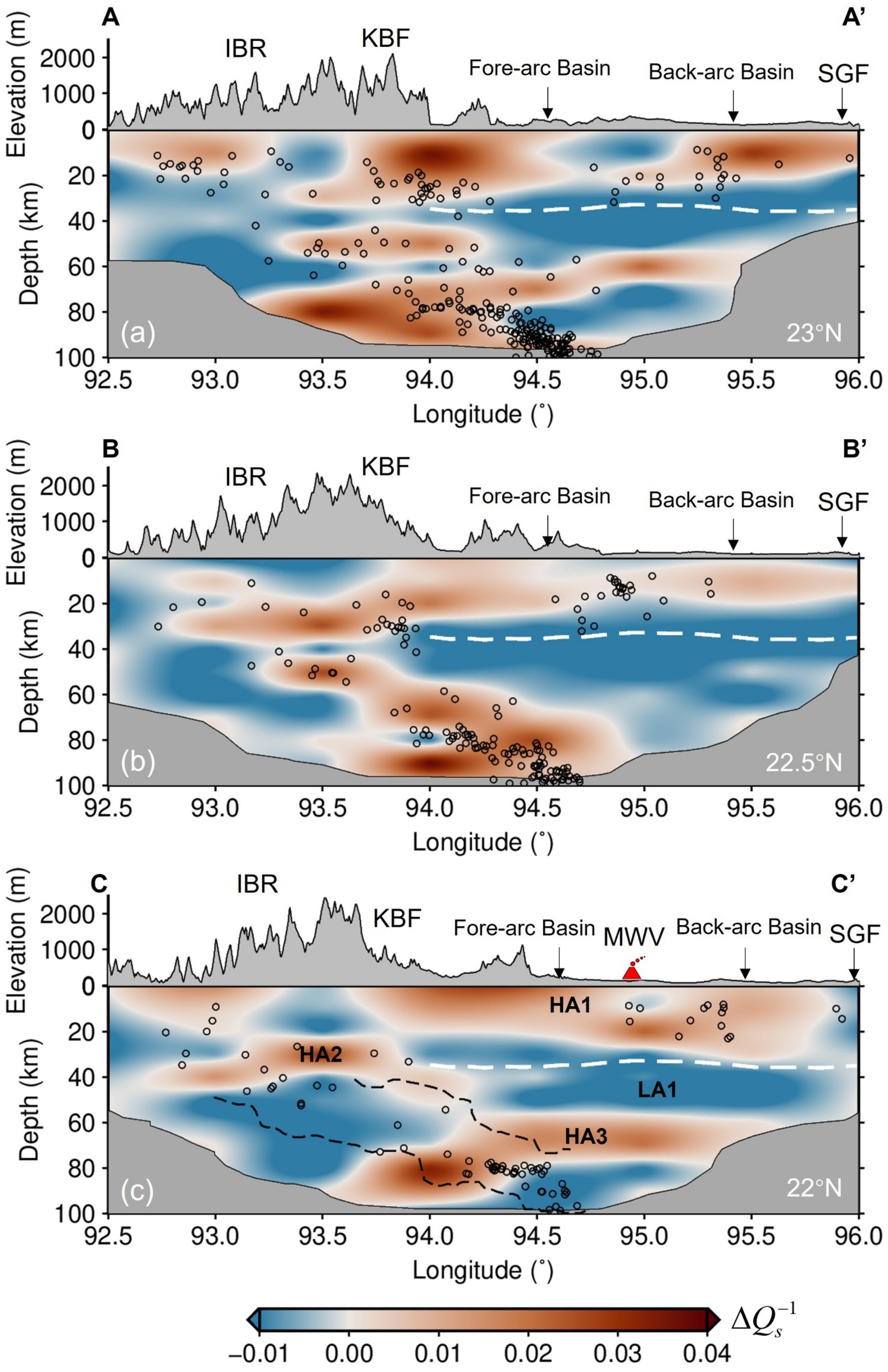

Figure 4. S-wave attenuation profiles along (a) 23°N, (b) 22.5°N, and (c) 22°N, respectively, where relatively high-attenuation zones are labeled as HA1, HA2, HA3, and a low-attenuation zone as LA1. The black dots indicate the earthquakes relocated at the imaging latitude within a range of ±0.25° from individual profiles (Mon et al., 2020, 2023). Areas with lower resolution are marked in gray. The black dashed lines in Panel (c) represent the crust of the subducting Indian plate (T. Zheng et al., 2020). The dashed white lines indicate the Moho depths obtained from CRUST 1.0 (Laske et al., 2013). IBR: Indo-Burma Ranges; KBF: Kabaw Fault; SGF: Sagaing Fault; MWV: Monywa volcano.

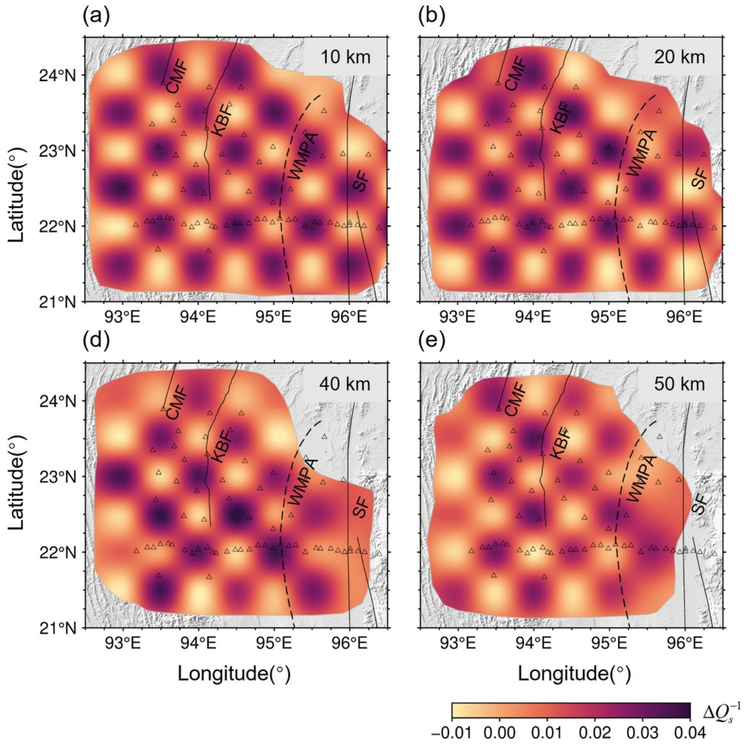

Figure 5. The checkerboard tests at depths of (a) 10 km, (b) 20 km, (c) 30 km, (d) 40 km, (e) 50 km, and (f) 60 km, respectively.

distribution, indicating that our inversion results are unbiased with respect to systematic errors and that the inversion is therefore stable.

To prevent strong wave propagation effects associated with the Moho and near-source shallow structures, we conducted additional tests for 3D attenuation tomography, using the same parameters based on data from earthquakes with focal depths greater than 60 km. The results show that the main structures we discuss exhibit slight changes from those obtained from all seismic events (Figure S11 in Supporting Information S1), while changes in the shallow structure are due to insufficient ray coverage (Figure S12 in Supporting Information S1). This test proves the stability of the results obtained across the lower crust and uppermost mantle.

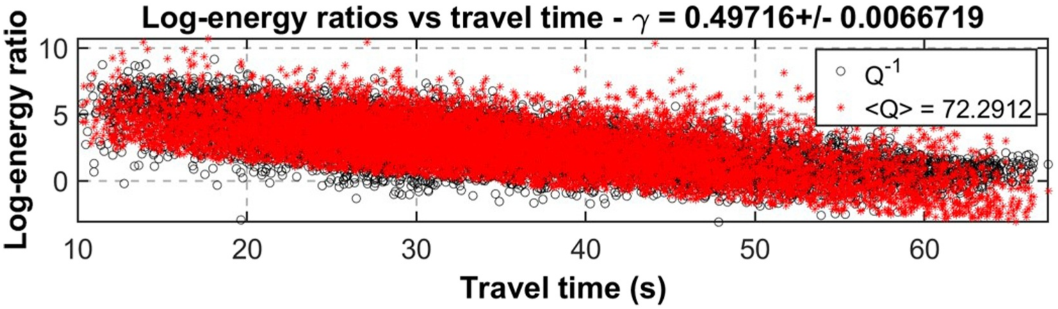

Figure 6. The log energy ratios versus travel time. The black dots represent the observed data, which are compared with the predicted data (red stars) obtained after inverting for the geometrical spreading factor γ and the average Q. Average quality factor 72.2912 and geometrical spreading 0.49716 ± 0.0066719.

4. Discussion

4.1. Comparison With Previous Studies

We compare our seismic attenuation model with existing seismic velocity models (Bai et al., 2021; S. Wu et al., 2021; G. Zhang et al., 2021). The high attenuation observed within the CMB aligns with its low-velocity structure and is consistent with the sedimentary basin thickness inferred from seismic reflection profiles (Pivnik et al., 1998) (Figures 3a, 3b and 4a–4c). This attenuation anomaly, characteristic of sedimentary basins (Borleanu et al., 2023), further supports the conclusion that the fore-arc basin exhibits a greater sedimentary thickness relative to the back-arc basin (Bai et al., 2021; S. Wu et al., 2021; G. Zhang et al., 2021). Our results are also consistent with those of R. S. Wu et al. (2007), who identified high attenuation in the Myanmar block at low frequencies. This was interpreted as a result of a thick sedimentary layer or the boundary between the lowlands and surrounding mountains, causing significant scattering of Lg waves. The presence of both high-attenuation and low-velocity anomalies strengthens the inference that Myanmar has a significant sedimentary cover, including two fault zones in the CMB (as determined by seismic relocations by Mon et al., 2020) and high Vp/Vs in the basin (G. Zhang et al., 2021), which may be fluid-rich.

The IBR was initially formed in an accretionary prism setting. Subsequently, it evolved into a subaerial fold-and-thrust belt during the highly oblique collision between Sundaland and the Indian Plate (Morley et al., 2020). It is commonly divided into three zones: an outer Western Belt, characterized by detached fold and thrust systems developed primarily in Neogene sediments; an inner Eastern Belt, characterized by a folded and thrusted region of predominantly Late Cretaceous-Palaeogene section; and the "Core," the most easterly and tectonically complex zone, which marks a broad suture zone of Tethys ocean and related back-arc basin-derived rock units (Licht et al., 2019; Maurin & Rangin, 2009; Morley et al., 2020). In addition, our attenuation tomography reveals a strong north-south-trending attenuation anomaly parallel to the subduction plates in the mid-to-lower crust of the IBR (Figure 3c), which spatially coincides with a low-velocity anomaly (*Vs* of ~3.2 km/s) previously identified at a similar position (Bai et al., 2020; Raoof et al., 2017; S. Wu et al., 2021). This result supports the existence of a consistent sedimentary coverage in the accretionary wedge that, during the subduction of the Indian plate, is progressively transported into the mid-to-lower crust. It is also indicative of high fluid content in the accreted/underplated sediments, as well as from the subducting plate, which may further reduce the adequate strength of the crust and facilitate deformation in the IBR.

4.2. Magmatic Activity at Monywa Volcano

MWV was formed as a result of east-dipping subduction of the Indian plate and is located at the central axis of the CMB (Cai et al., 2020; Oo et al., 2021; Y. Wang et al., 2014). Beneath active volcanic arcs, evidence of partially molten and fluid-saturated regions is extensive, leading to significant seismic attenuation and absorption (D. Liu et al., 2024, H. Liu et al., 2024; Reiss et al., 2022; Roth et al., 1999; Tsumura et al., 2000; Zhao, 2001). Geochemical studies have revealed that the volcanic activity at the MWV can be divided into two distinct stages: the middle Miocene and the Quaternary. The mid-Miocene rocks show typical arc lava characteristics, that is, large ion lithophile element enrichments and high field strength element depletions. During the Quaternary stage, the volcanism displays significant geochemical heterogeneity, with the alkali basalt suite II interpreted as the product of partial melting from the asthenosphere (Lee et al., 2016). Our results reveal that, while most of the crust exhibits high attenuation, as expected for a volcanic region, a zone of weak attenuation is present at depths of 30–50 km (Figure 4c). Previous velocity tomography studies have generally interpreted a small-scale, low-velocity body immediately under the sub-arc Moho as a small magma pocket (Bai et al., 2021; G. Zhang et al., 2021; T. Zheng et al., 2020). We thus infer a relatively small magma source volume, which is consistent with the lack of strong attenuation zones typically observed near volcanic arcs with limited melt supply. As a result, even where limited heat sources and partial melting exist, magma may remain trapped at depth and fail to rise effectively. Therefore, the combined observations of weak attenuation and small-scale, low-velocity bodies within the 30–50 km depth range suggest a stable lithospheric block.

In contrast to the low attenuation observed in the depth range of 30–50 km, a high attenuation anomaly is observed below 50 km, which corresponds to the low-velocity body beneath the volcanic arc identified in seismic tomography (G. Zhang et al., 2021). This anomaly likely marks hot mantle material formed by asthenospheric upwelling, either due to a tear in the subducting slab (Bai et al., 2020; L. Y. Zhang et al., 2020) or due to thermal processes (He et al., 2021). The MWV has experienced at least two phases of eruptive activity. We know that the

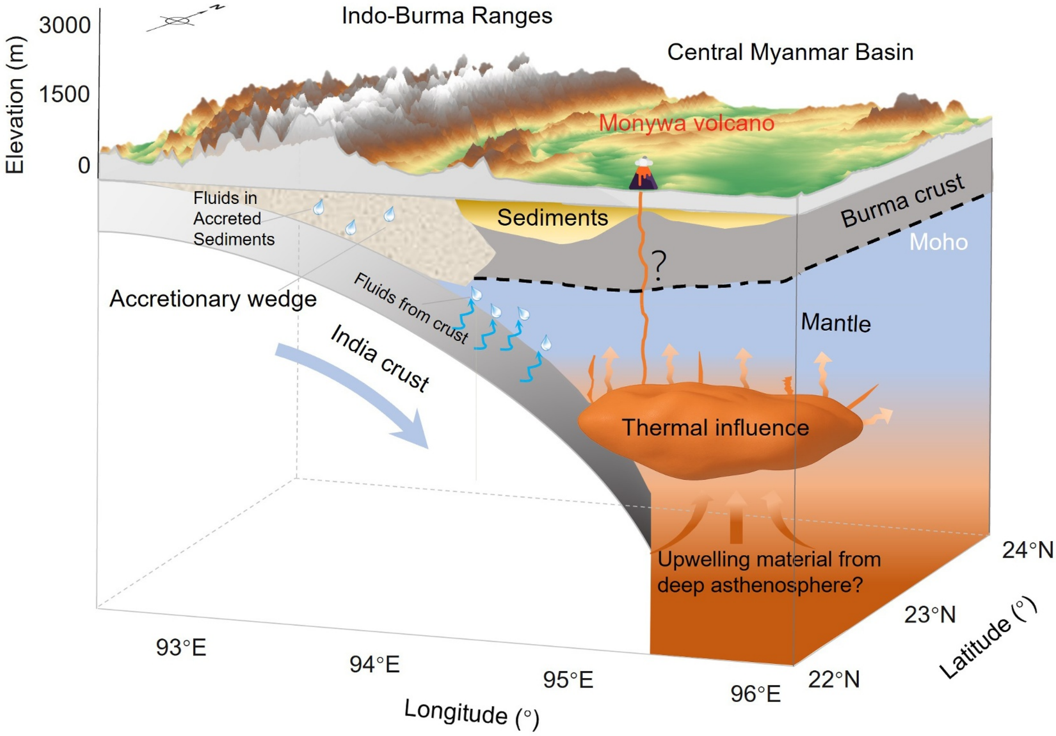

Figure 7. Schematic illustration of the Indo-Burma subduction zone based on our imaging results. The diagram depicts the crustal and mantle structure beneath the MWV, highlighting the attenuation characteristics of the subduction zone, which include the cold subducting crust, limited mantle wedge melting due to slab dehydration, and fluid-rich sediments from the Indo-Burma Ranges entering the lower crust.

primary material of the volcano is derived from mantle source rocks from geochemical results, and the upwelling of deep asthenosphere material may indeed be related to such slab-tearing events (Bai et al., 2020; L. Y. Zhang et al., 2020); however, given the small-scale of such tearing, it might have only induced a limited thermal perturbation (He et al., 2021). We cannot definitively exclude the influence of deeper mantle processes, such as mantle plumes or slab rollback. These processes may heat parts of the crystallized mush system, triggering renewed volcanic activity in Pliocene and Pleistocene volcanoes, and possibly allowing magma to rise to the surface through weak zones or cracks in the lithosphere (Figure 7). Due to the limited resolution, we cannot effectively constrain the upwelling magma conduits or thermal sources below a depth of 70 km. Future studies incorporating higher-resolution seismic imaging and thermal modeling are needed to further investigate the origin and evolution of the deep magmatic system beneath MWV.

4.3. Continental Subduction System of the Indo-Burma Subduction Zone

The identification of the IBSZ as a result of continental subduction is supported by both receiver function analysis (T. Zheng et al., 2020), which reveals a subducting crust with a crustal thickness of approximately 30 km, and seismic tomography, which indicates a low-velocity crust of the subducting plate (G. Zhang et al., 2021). Previous high-resolution attenuation tomography studies of subduction zones have focused on oceanic systems, such as those in Japan (Kita et al., 2014; X. Liu et al., 2014; X. Liu & Zhao, 2014), Sumatra (D. Liu et al., 2024, H. Liu et al., 2024), Tonga (Wei & Wiens, 2018), the Andes (Schurr et al., 2003), New Zealand (Eberhart-Phillips et al., 2020), and the Lesser Antilles (Hicks et al., 2023). These previous studies consistently image weakly attenuating subducting slabs and strongly attenuating mantle wedge melting zones associated with volcanic arcs and back-arc regions. Velocity tomography in these oceanic settings typically reveals high-velocity subducting slabs and low-velocity, melt-rich mantle wedges (Bie et al., 2022; Zhao et al., 1997). In contrast, our previous velocity tomography shows a low-velocity zone associated with the subducting continental crust. At the same time, our attenuation results reveal a high-attenuation anomaly beneath the fore-arc region of the IBSZ dipping at an angle nearly parallel to the subducting crust (Figures 4a–4c). In oceanic subduction zones, Q values within the slab are generally 400–600 (Kita et al., 2014), while those in the mantle wedge are much lower due to extensive partial melting. In our study area, however, the region overlying the subducting continental slab exhibits a lower Q value, whereas the region beneath the volcanic arc is characterized by relatively high Q values. Moreover, convergence rate may exert a significant control on slab-derived fluid flux. In rapidly converging oceanic subduction settings, fluids released through slab dehydration can be transported to the overlying mantle wedge within ~30–50 kyr, where they trigger partial melting (Turner & Hawkesworth, 1997), subsequently giving rise to intense back-arc volcanism and the formation of dense volcanic chains (D. Liu et al., 2024, H. Liu et al., 2024). In contrast, within the IBSZ, the relatively slow convergence rate markedly reduces the efficiency of fluid transport, thereby limiting magmatic activity (Belousov et al., 2018; Panda et al., 2020). Comparing our 3D attenuation results with velocity tomography, we propose that the high-attenuation anomaly may be caused by fluids released from the dehydrating subducting continental crust, leading to limited partial melting overlying the subducting continental crust. Given the overall low water content of the subducting continental crust, the scale of melting is restricted, resulting in the absence of continuous pathways linking deep thermal sources to volcanic centers. This limited melting is reflected in the attenuation characteristics of the IBSZ, which differ significantly from those observed in typical oceanic subduction zones (Kita et al., 2014; Stachnik et al., 2004). Additionally, the oceanic subducting lithosphere is relatively thin and enriched in hydrous minerals such as serpentine and amphibole, which undergo dehydration at relatively shallow depths (tens to a few hundred kilometers) (Christensen & Salisbury, 1975; Rudnick & Fountain, 1995). The released fluids are efficiently transported along permeable channels, enabling heating and partial melting of the mantle wedge and consequently giving rise to active volcanic arcs and continuous volcanic chains. In contrast, in continental subduction zones, the crust is significantly thicker, and hydrous minerals, such as mica and amphibole, exhibit different distributions and stabilities (Rudnick & Fountain, 1995). Dehydration reactions occur at greater depths and in a more discontinuous manner. Furthermore, the thermal coupling between the subducting slab and the overlying mantle or crust is less efficient, which further suppresses melt generation (Y. F. Zheng & Chen, 2016). There is no evidence that the MWV has erupted since the Holocene (Belousov et al., 2018), indirectly suggesting that the underlying upper mantle is now characterized by a cold and stable tectonic regime (Figure 7). Figure 7 shows a cartoon based on velocity tomography (Figure S13 in Supporting Information S1) and our results, illustrating the IBSZ and highlighting the absence of recent eruptive activity.

5. Conclusion

This study presents a high-resolution S-wave attenuation model of the lithosphere in Myanmar, obtained by employing the CN method on regional earthquake data. Our results reveal the following key points: (a) Widespread high-attenuation anomalies are identified beneath the CMB and the IBR, corresponding to thick sedimentary sequences and fluid-rich accretionary wedges, respectively. (b) A pronounced high-attenuation anomaly appears below 50 km, suggesting the upwelling of asthenospheric material potentially associated with slab tearing or retreat of the subducting Indian plate. (c) Our study reveals distinct attenuation characteristics in this continental subduction setting, where limited high-attenuation anomalies are observed overlying the low-attenuation subducting crust, suggesting that the lower water content and limited degree of melting are insufficient to induce widespread attenuation in the back-arc region.

Conflict of Interest

The authors declare no conflicts of interest relevant to this study.

Data Availability Statement

The waveform data used for CN analysis in this study, collected from the recently deployed first phase of the CMGSMO seismic array, are available at Feng et al. (2025). The software Murat3.0, the third release of an open-access code (De Siena et al., 2024), used to perform attenuation imaging of this area, is available at the Zenodo repository (https://doi.org/10.5281/zenodo.13996752). The software was used to obtain Figures 2 and 6. Figures 1 and 3–5 were generated using GMT 6 (Wessel et al., 2019), which is accessible and downloadable at https://www.generic-mapping-tools.org/download/, and custom-written Python scripts.

Acknowledgments

We gratefully acknowledge the researchers and colleagues at the Seismic Array Laboratory, Institute of Geology and Geophysics, Chinese Academy of Sciences, for their efforts in installing and maintaining the CMGSMO seismic network. We thank Wei Wang for the valuable discussion. This study is supported by the National Natural Science Foundation of China (Grants 42030309 and 42130308). We thank Editor Fenglin Niu, the Associate Editor, Reviewer Tuna Eken, and an anonymous reviewer for their helpful comments, which significantly improved the presentation of our results.

References

Aki, K. (1980). Scattering and attenuation of shear waves in the lithosphere. *Journal of Geophysical Research*, *85*(B11), 6496–6504. https://doi.org/10.1029/JB085iB11p06496

Aki, K., & Chouet, B. (1975). Origin of coda waves: Source, attenuation, and scattering effects. *Journal of Geophysical Research*, *80*(23), 3322–3342. https://doi.org/10.1029/JB080i023p03322

Bai, Y., He, Y., Yuan, X., Tilmann, F., Ai, Y., Jiang, M., et al. (2021). Seismic structure across central Myanmar from joint inversion of receiver functions and Rayleigh wave dispersion. *Tectonophysics*, *818*, 229068. https://doi.org/10.1016/j.tecto.2021.229068

Bai, Y., Yuan, X., He, Y., Hou, G., Thant, M., Sein, K., & Ai, Y. (2020). Mantle transition zone structure beneath Myanmar and its geodynamic implications. *Geochemistry, Geophysics, Geosystems*, *21*(12), e2020GC009262. https://doi.org/10.1029/2020GC009262

Belousov, A., Belousova, M., Zaw, K., Streck, M. J., Bindeman, I., Meffre, S., & Vasconcelos, P. (2018). Holocene eruptions of Mt. Popa, Myanmar: Volcanological evidence of the ongoing subduction of Indian plate along Arakan Trench. *Journal of Volcanology and Geothermal Research*, *360*, 126–138. https://doi.org/10.1016/j.jvolgeores.2018.06.010

Bie, L., Hicks, S., Rietbrock, A., Goes, S., Collier, J., Rychert, C., et al. (2022). Imaging slab-transported fluids and their deep dehydration from seismic velocity tomography in the lesser antilles subduction zone. *Earth and Planetary Science Letters*, *586*, 117535. https://doi.org/10.1016/j.epsl.2022.117535

Borleanu, F., Petrescu, L., Seghedi, I., Thomas, C., & De Siena, L. (2023). The seismic attenuation signature of collisional orogens and sedimentary basins within the carpathian orogen. *Global and Planetary Change*, *223*, 104093. https://doi.org/10.1016/j.gloplacha.2023.104093

Boyd, O. S., Jones, C. H., & Sheehan, A. F. (2004). Foundering lithosphere imaged beneath the Southern Sierra Nevada, California, USA. *Science*, *305*(5684), 660–662. https://doi.org/10.1126/science.1099181

Cai, F., Ding, L., Zhang, Q., Orme, D. A., Wei, H., Li, J., et al. (2020). Initiation and evolution of forearc basins in the central Myanmar depression. *Geological Society of America Bulletin*, *132*(5–6), 1066–1082. https://doi.org/10.1130/B35301.1

Christensen, N. I., & Salisbury, M. H. (1975). Structure and constitution of the lower oceanic crust. *Reviews of Geophysics*, *13*(1), 57–86. https://doi.org/10.1029/RG013i001p00057

Del Pezzo, E., Bianco, F., De Siena, L., & Zollo, A. (2006). Small scale shallow attenuation structure at mt. Vesuvius, Italy. *Physics of the Earth and Planetary Interiors*, *157*(3–4), 257–268. https://doi.org/10.1016/j.pepi.2006.04.009

De Siena, L., Amoruso, A., Pezzo, E. D., Wakeford, Z., Castellano, M., & Crescentini, L. (2017). Space-weighted seismic attenuation mapping of the aseismic source of Campi Flegrei 1983–1984 unrest. *Geophysical Research Letters*, *44*(4), 1740–1748. https://doi.org/10.1002/2017GL072507

De Siena, L., Chiodini, G., Vilardo, G., Del Pezzo, E., Castellano, M., Colombelli, S., et al. (2017). Source and dynamics of a volcanic caldera unrest: Campi Flegrei, 1983–84. *Scientific Reports*, *7*(1), 8099. https://doi.org/10.1038/s41598-017-08192-7

De Siena, L., Del Pezzo, E., & Bianco, F. (2010). Seismic attenuation imaging of Campi Flegrei: Evidence of gas reservoirs, hydrothermal basins, and feeding systems. *Journal of Geophysical Research*, *115*(B9), B09312. https://doi.org/10.1029/2009JB006938

De Siena, L., Del Pezzo, E., Bianco, F., & Tramelli, A. (2009). Multiple resolution seismic attenuation imaging at mt. Vesuvius. *Physics of the Earth and Planetary Interiors*, *173*(1–2), 17–32. https://doi.org/10.1016/j.pepi.2008.10.015

De Siena, L., Mreissuf, Zhang, Y., GeoSeisUtilities, Abbas, A., Wmz, et al. (2024). LucaDeSiena/MuRAT: 3.24.10.26 (v3.24.10.26). *Zenodo*. https://doi.org/10.5281/zenodo.13996752

De Siena, L., Thomas, C., & Aster, R. (2014). Multi-scale reasonable attenuation tomography analysis (MuRAT): An imaging algorithm designed for volcanic regions. *Journal of Volcanology and Geothermal Research*, *277*, 22–35. https://doi.org/10.1016/j.jvolgeores.2014.03.009

Eberhart-Phillips, D., Bannister, S., & Reyners, M. (2020). Attenuation in the mantle wedge beneath super-volcanoes of the Taupo volcanic zone, New Zealand. *Geophysical Journal International*, *220*(1), 703–723. https://doi.org/10.1093/gji/ggz455

Feng, Y., Ai, Y., Luca, D. S., He, Y., Jiang, M., Chit, T. M., et al. (2025). Seismic attenuation tomography data for lithosphere structure investigation in Central Myanmar [Dataset]. https://doi.org/10.12197/2025GA014

Gabrielli, S., Akinci, A., & Del Pezzo, E. (2025). Temporal and spatial variability of S-wave and coda attenuation in the central Apennines, Italy. *Frontiers in Earth Science*, *12*, 1487797. https://doi.org/10.3389/feart.2024.1487797

Gabrielli, S., De Siena, L., Napolitano, F., & Del Pezzo, E. (2020). Understanding seismic path biases and magmatic activity at Mount St Helens volcano before its 2004 eruption. *Geophysical Journal International*, *222*(1), 169–188. https://doi.org/10.1093/gji/ggaa154

He, X., Zhao, L.-F., Xie, X.-B., Tian, X., & Yao, Z.-X. (2021). Weak crust in Southeast Tibetan Plateau revealed by Lg-Wave attenuation tomography: Implications for crustal material escape. *Journal of Geophysical Research: Solid Earth*, *126*(3), e2020JB020748. https://doi.org/10.1029/2020JB020748

Hicks, S. P., Bie, L., Rychert, C. A., Harmon, N., Goes, S., Rietbrock, A., et al. (2023). Slab to back-arc to arc: Fluid and melt pathways through the mantle wedge beneath the Lesser Antilles. *Science Advances*, *9*(5), eadd2143. https://doi.org/10.1126/sciadv.add2143

Kita, S., Nakajima, J., Hasegawa, A., Okada, T., Katsumata, K., Asano, Y., & Kimura, T. (2014). Detailed seismic attenuation structure beneath Hokkaido, northeastern Japan: Arc-arc collision process, arc magmatism, and seismotectonics. *Journal of Geophysical Research: Solid Earth*, *119*(8), 6486–6511. https://doi.org/10.1002/2014JB011099

Laske, G., Masters, G., Ma, Z., & Pasyanos, M. (2013). Update on CRUST1.0 - A 1-degree global model of Earth's crust. In *EGU General Assembly conference abstracts*. Retrieved from http://igppweb.ucsd.edu/~gabi/rem.html

Lee, H.-Y., Chung, S.-L., & Yang, H.-M. (2016). Late Cenozoic volcanism in central Myanmar: Geochemical characteristics and geodynamic significance. *Lithos*, *245*, 174–190. https://doi.org/10.1016/j.lithos.2015.09.018

Licht, A., Dupont-Nivet, G., Win, Z., Swe, H. H., Kaythi, M., Roperch, P., et al. (2019). Paleogene evolution of the Burmese forearc basin and implications for the history of India-Asia convergence. *GSA Bulletin*, *131*(5–6), 730–748. https://doi.org/10.1130/B35002.1

Licht, A., Win, Z., Westerweel, J., Cogné, N., Morley, C. K., Chantraprasert, S., et al. (2020). Magmatic history of central Myanmar and implications for the evolution of the Burma Terrane. *Gondwana Research*, *87*, 303–319. https://doi.org/10.1016/j.gr.2020.06.016

Liu, D., Wang, Z., Zhao, D., Hu, H., & Gao, R. (2024). Accretionary wedge, arc magmatism and fluid migration in Northern Sumatra: Insight from seismic attenuation tomography. *Journal of Geophysical Research: Solid Earth*, *129*(12), e2024JB029777. https://doi.org/10.1029/2024JB029777

Liu, H., Pei, S., Liu, W., Xue, X., Li, J., Hua, Q., & Li, L. (2024). Crustal and upper mantle attenuation structure beneath the Southeastern Tibetan Plateau and its implications on Plateau outgrowth. *Journal of Geophysical Research: Solid Earth*, *129*(2), e2023JB026977. https://doi.org/10.1029/2023JB026977

Liu, X., & Zhao, D. (2014). Structural control on the nucleation of megathrust earthquakes in the Nankai subduction zone. *Geophysical Research Letters*, *41*(23), 8288–8293. https://doi.org/10.1002/2014GL062002

Liu, X., Zhao, D., & Li, S. (2014). Seismic attenuation tomography of the Northeast Japan arc: Insight into the 2011 Tohoku earthquake (Mw 9.0) and subduction dynamics. *Journal of Geophysical Research: Solid Earth*, *119*(2), 1094–1118. https://doi.org/10.1002/2013jb010591

Maurin, T., & Rangin, C. (2009). Structure and kinematics of the Indo-Burmese Wedge: Recent and fast growth of the outer wedge. *Tectonics*, *28*(2), 2008TC002276. https://doi.org/10.1029/2008TC002276

Metcalfe, I. (2013). Gondwana dispersion and asian accretion: Tectonic and palaeogeographic evolution of eastern tethys. *Journal of Asian Earth Sciences*, *66*, 1–33. https://doi.org/10.1016/j.jseaes.2012.12.020

Mitchell, A., Chung, S.-L., Oo, T., Lin, T.-H., & Hung, C.-H. (2012). Zircon U–Pb ages in Myanmar: Magmatic–metamorphic events and the closure of a neo-tethys ocean? *Journal of Asian Earth Sciences*, *56*, 1–23. https://doi.org/10.1016/j.jseaes.2012.04.019

Mon, C. T., Gong, X., Wen, Y., Jiang, M., Chen, Q.-F., Zhang, M., et al. (2020). Insight into major active faults in central Myanmar and the related geodynamic sources. *Geophysical Research Letters*, *47*(8), e2019GL086236. https://doi.org/10.1029/2019GL086236

Mon, C. T., Yang, S., Ren, C., He, Y., Thant, M., & Sein, K. (2023). New Insight into the subducted Indian plate beneath central Myanmar based on seismic activity and focal mechanisms analysis. *Seismological Research Letters*, *94*(5), 2337–2347. https://doi.org/10.1785/0220220381

Morley, C. K., Tin, T. N., Searle, M., & Robinson, S. A. (2020). Structural and tectonic development of the Indo-Burma ranges. *Earth-Science Reviews*, *200*, 102992. https://doi.org/10.1016/j.earscirev.2019.102992

Oo, T. N., Harijoko, A., & Setijadji, L. D. (2021). Petrographic characteristics and geochemistry of volcanic rocks in the kyaukmyet prospect, Monywa district, Central Myanmar. *Journal of Geological Research*, *3*(4). https://doi.org/10.30564/jgr.v3i4.3605

Panda, D., Kundu, B., Gahalaut, V. K., & Rangin, C. (2020). India-sunda plate motion, crustal deformation, and seismic hazard in the indo-burmese arc. *Tectonics*, *39*(8), e2019TC006034. https://doi.org/10.1029/2019TC006034

Pivnik, D. A., Nahm, J., & Tuck, R. S. (1998). Polyphase deformation in a fore-arc/back-arc basin, Salin Subbasin, Myanmar (Burma). *AAPG Bulletin*, *82*(1998). https://doi.org/10.1306/1D9BD15F-172D-11D7-8645000102C1865D

Prudencio, J., De Siena, L., Ibáñez, J. M., Del Pezzo, E., García-Yeguas, A., & Díaz-Moreno, A. (2015). The 3D attenuation structure of deception Island (Antarctica). *Surveys in Geophysics*, *36*(3), 371–390. https://doi.org/10.1007/s10712-015-9322-6

Rao, C. K., Selvaraj, C., & Gokarn, S. G. (2014). Deep electrical structure over the igneous arc of the Indo Burman Orogen in Sagaing province, Myanmar from magnetotelluric studies. *Journal of Asian Earth Sciences*, *94*, 68–76. https://doi.org/10.1016/j.jseaes.2014.08.016

Raoof, J., Mukhopadhyay, S., Koulakov, I., & Kayal, J. R. (2017). 3-D seismic tomography of the lithosphere and its geodynamic implications beneath the northeast India region. *Tectonics*, *36*(5), 962–980. https://doi.org/10.1002/2016TC004375

Reiss, M. C., De Siena, L., & Muirhead, J. D. (2022). The interconnected magmatic plumbing System of the natron rift. *Geophysical Research Letters*, *49*(15), e2022GL098922. https://doi.org/10.1029/2022GL098922

Roth, E. G., Wiens, D. A., Dorman, L. M., Hildebrand, J., & Webb, S. C. (1999). Seismic attenuation tomography of the Tonga-Fiji region using phase pair methods. *Journal of Geophysical Research*, *104*(B3), 4795–4809. https://doi.org/10.1029/1998JB900052

Rudnick, R. L., & Fountain, D. M. (1995). Nature and composition of the continental crust: A lower crustal perspective. *Reviews of Geophysics*, *33*(3), 267–309. https://doi.org/10.1029/95RG01302

Sato, H., Fehler, M. C., & Maeda, T. (2012). *Seismic wave propagation and scattering in the heterogeneous Earth: Second edition*. Springer Berlin Heidelberg. https://doi.org/10.1007/978-3-642-23029-5

Schurr, B., Asch, G., Rietbrock, A., Trumbull, R., & Haberland, C. (2003). Complex patterns of fluid and melt transport in the central Andean subduction zone revealed by attenuation tomography. *Earth and Planetary Science Letters*, *215*(1–2), 105–119. https://doi.org/10.1016/S0012-821X(03)00441-2

Sketsiou, P., De Siena, L., Gabrielli, S., & Napolitano, F. (2021). 3-D attenuation image of fluid storage and tectonic interactions across the Pollino fault network. *Geophysical Journal International*, *226*(1), 536–547. https://doi.org/10.1093/gji/ggab109

Stachnik, J. C., Abers, G. A., & Christensen, D. H. (2004). Seismic attenuation and mantle wedge temperatures in the Alaska subduction zone. *Journal of Geophysical Research*, *109*(B10), 2004JB003018. https://doi.org/10.1029/2004JB003018

Takemura, S., Furumura, T., & Saito, T. (2009). Distortion of the apparent S-wave radiation pattern in the high-frequency wavefield: Tottori-ken Seibu, Japan, earthquake of 2000. *Geophysical Journal International*, *178*(2), 950–961. https://doi.org/10.1111/j.1365-246X.2009.04210.x

Tian, Y., Jiang, M., He, Y., Ai, Y., Hou, G., Ling, Y., et al. (2024). Termination of Mid-to-lower crustal extrusion on the Eastern flank of the Eastern Himalayan syntaxis: Implied from trans-regional ambient noise tomography. *Geophysical Research Letters*, *51*(15), e2024GL108740. https://doi.org/10.1029/2024GL108740

Tsumura, N., Matsumoto, S., Horiuchi, S., & Hasegawa, A. (2000). Three-dimensional attenuation structure beneath the northeastern Japan arc estimated from spectra of small earthquakes. *Tectonophysics*, *319*(4), 241–260. https://doi.org/10.1016/S0040-1951(99)00297-8

Turner, S., & Hawkesworth, C. (1997). Constraints on flux rates and mantle dynamics beneath island arcs from Tonga–kermadec lava geochemistry. *Nature*, *389*(6651), 568–573. https://doi.org/10.1038/39257

Um, J., & Thurber, C. (1987). A fast algorithm for two-point seismic ray tracing. *Bulletin of the Seismological Society of America*, *77*(3), 972–986. https://doi.org/10.1785/BSSA0770030972

Wang, X., Wei, S., Wang, Y., Maung Maung, P., Hubbard, J., Banerjee, P., et al. (2019). A 3-D shear wave velocity model for Myanmar region. *Journal of Geophysical Research: Solid Earth*, *124*(1), 504–526. https://doi.org/10.1029/2018JB016622

Wang, Y., Sieh, K., Tun, S. T., Lai, K., & Myint, T. (2014). Active tectonics and earthquake potential of the Myanmar region. *Journal of Geophysical Research: Solid Earth*, *119*(4), 3767–3822. https://doi.org/10.1002/2013JB010762

Wei, S. S., & Wiens, D. A. (2018). P-wave attenuation structure of the Lau back-arc basin and implications for mantle wedge processes. *Earth and Planetary Science Letters*, *502*, 187–199. https://doi.org/10.1016/j.epsl.2018.09.005

Wessel, P., Luis, J. F., Uieda, L., Scharroo, R., Wobbe, F., Smith, W. H. F., & Tian, D. (2019). The generic mapping tools version 6. *Geochemistry, Geophysics, Geosystems*, *20*(11), 5556–5564. https://doi.org/10.1029/2019GC008515

Wu, R.-S., Wu, X.-Y., & Xie, X.-B. (2007). Simulation of high-frequency wave propagation in complex crustal waveguides using generalized screen propagators. In *Advances in geophysics* (Vol. 48, pp. 323–363). Elsevier. https://doi.org/10.1016/S0065-2687(06)48006-7

Wu, S., Yao, J., Wei, S., Hubbard, J., Wang, Y., Min Htwe, Y. M., et al. (2021). New insights into the structural heterogeneity and geodynamics of the Indo-Burma subduction zone from ambient noise tomography. *Earth and Planetary Science Letters*, *562*, 116856. https://doi.org/10.1016/j.epsl.2021.116856

Yoshimoto, K., Sato, H., & Ohtake, M. (1993). Frequency-dependent attenuation of *P* and *S* waves in the Kanto area, Japan, based on the coda-normalization method. *Geophysical Journal International*, *114*(1), 165–174. https://doi.org/10.1111/j.1365-246X.1993.tb01476.x

Zhang, G., He, Y., Ai, Y., Jiang, M., Mon, C. T., Hou, G., et al. (2021). Indian continental lithosphere and related volcanism beneath Myanmar: Constraints from local earthquake tomography. *Earth and Planetary Science Letters*, *567*, 116987. https://doi.org/10.1016/j.epsl.2021.116987

Zhang, L. Y., Fan, W. M., Ding, L., Ducea, M. N., Pullen, A., Li, J. X., et al. (2020). Quaternary volcanism in Myanmar: A record of Indian slab tearing in a transition zone from Oceanic to Continental subduction. *Geochemistry, Geophysics, Geosystems*, *21*(8), e2020GC009091. https://doi.org/10.1029/2020GC009091

Zhao, D. (2001). Seismological structure of subduction zones and its implications for arc magmatism and dynamics. *Physics of the Earth and Planetary Interiors*, *127*(1–4), 197–214. https://doi.org/10.1016/S0031-9201(01)00228-X

Zhao, D., Xu, Y., Wiens, D. A., Dorman, L., Hildebrand, J., & Webb, S. (1997). Depth extent of the lau back-arc spreading center and its relation to subduction processes. *Science*, *278*(5336), 254–257. https://doi.org/10.1126/science.278.5336.254

Zheng, T., He, Y., Ding, L., Jiang, M., Ai, Y., Mon, C. T., et al. (2020). Direct structural evidence of Indian continental subduction beneath Myanmar. *Nature Communications*, *11*(1), 1944. https://doi.org/10.1038/s41467-020-15746-3

Zheng, Y.-F., & Chen, Y.-X. (2016). Continental versus oceanic subduction zones. *National Science Review*, *3*(4), 495–519. https://doi.org/10.1093/nsr/nww049